

**Self-Assembled FeS<sub>2</sub> Cubes Anchored on Reduced Graphene Oxide as Anode Material for Lithium Ion Batteries**

Journal:	<i>Journal of Materials Chemistry A</i>
Manuscript ID:	TA-ART-10-2014-005575.R1
Article Type:	Paper
Date Submitted by the Author:	27-Nov-2014
Complete List of Authors:	Wen, Xun; Xiangtan University, Wei, Xiao-Lin; Xiangtan University, Yang, Liwen; Faculty of Materials and Optoelectronic Physics, Xiangtan University, Shen, Pei; Sun Yat-sen University,

Cite this: DOI: 10.1039/c0xx00000x

www.rsc.org/xxxxxx

ARTICLE TYPE

# Self-Assembled FeS<sub>2</sub> Cubes Anchored on Reduced Graphene Oxide as Anode Material for Lithium Ion Batteries

Xun Wen,<sup>a</sup> Xiaolin Wei,<sup>\*a</sup> Liwen Yang<sup>a</sup> and Pei Kang Shen,<sup>\*b</sup>*Received (in XXX, XXX) Xth XXXXXXXXX 20XX, Accepted Xth XXXXXXXXX 20XX*

DOI: 10.1039/b000000x

Novel composite of reduced graphene oxide (RGO) and FeS<sub>2</sub> microparticles self-assembled from small size cubes as a high-performance anode material for lithium-ion batteries (LIBs) have been prepared *via* a facile one-pot hydrothermal method. The prepared composite shows interconnected networks of reduced graphene oxide sheets and well-dispersed FeS<sub>2</sub> microparticles which were composed of small-size cubic FeS<sub>2</sub> crystals. The composite not only provides a high contact area between the electrolyte and electrode, favorable diffusion kinetics for both electrons and lithium ions, but also provides the protection against the volume changes of electroactive FeS<sub>2</sub> materials and excellent electrical conductivity of the overall electrode during electrochemical processes as well as enhanced synergistic effect between cubic FeS<sub>2</sub> and RGO. As an anode material for LIBs, it exhibits a very large initial reversible capacity of 1147 mAh g<sup>-1</sup> at a current rate of 100 mAh g<sup>-1</sup> and maintains 1001.41 mAh g<sup>-1</sup> over 60 cycles, which is much higher than that of the theoretical capacity of graphite (372 mAh g<sup>-1</sup>) and indicates high stability. The results demonstrate that the composite can be a promising candidate of electroactive materials for LIBs.

## 1. Introduction

Lithium-ion batteries (LIBs) have attracted extensive attention because of their high voltage, high specific energy, and long working life.<sup>1,2</sup> At present, their performance is approaching the achievable limits of the currently commercial graphite. To develop next generation LIBs with high energy density, many transition metal oxides<sup>3-6</sup> and sulfides<sup>7-11</sup> are researched as electrode materials in LIBs. Among of them, the FeS<sub>2</sub> has been recognized as one of the most promising anode materials for LIBs due to its unique features, such as high theoretical capacity of 890 mAh g<sup>-1</sup>, low environmental impact (non-toxic elements with respect to Fe and S) and affordable cost (abundant and cheap).<sup>12</sup> However, commercial FeS<sub>2</sub> suffers from poor cycling performance and low capacity retention due to lower conductivity and larger volume expansion during cycling processes, which prevents it from commercial application of LIBs.<sup>13,14</sup> To overcome those problems, various nano/micro structured FeS<sub>2</sub> materials such as nanorods, nanowires, nanocubes, nanoflakes and so on, have been synthesized to be used as high performance anodes.<sup>15-24</sup> Especially, sub-micrometer spherical materials with hierarchical structure are actually the optimal morphology in conventional electrode fabrication because these spherical particles not only have high packing density and good particle mobility to form a compact electrode layer but also can have less agglomeration and effectively avoid loosening and sloughing off. These features are beneficial to attain high volumetric energy and power density as well as uniform electrode layers.<sup>25</sup> Despite the progress via tuning the structure of the FeS<sub>2</sub>, the performance of the FeS<sub>2</sub>-based electrodes is still not satisfactory. It is highly desirable and big challenging to develop new strategies of constructing novel FeS<sub>2</sub>-based nanocomposites to further improve the anode performance. Recently, making nanocomposites involving highly conductive carbon has been proved to be effective for high-performance

FeS<sub>2</sub>-based electrode.<sup>14,26,27</sup> In particular, due to its excellent electrical conductivity, ultrashort pathway for Li<sup>+</sup> ions, large specific surface area, remarkable structural flexibility and prominent chemical stability and as a kind of novel two-dimensional carbon material, graphene or reduced graphene oxide (RGO) has been used as an ideal matrix for anchoring active nanomaterials such as SnO<sub>2</sub>,<sup>28</sup> TiO<sub>2</sub>,<sup>25</sup> CoO,<sup>29</sup> Fe<sub>2</sub>O<sub>3</sub>,<sup>30</sup> Li<sub>4</sub>Ti<sub>5</sub>O<sub>12</sub>,<sup>31</sup> and silicon,<sup>32</sup> to form the unique composite as electrode materials for LIBs with improved electrochemical performance.<sup>33</sup> It is expected that the hybrid electrodes of flexible and highly conductive graphene or RGO anchored with nano/micro structured FeS<sub>2</sub> can efficiently utilize the merits of both components, thereby exhibiting superior lithium storage performance. However, FeS<sub>2</sub>-based composite as an anode material for LIBs which combines the advantages of sub-micrometer spherically hierarchical structure and graphene or RGO, is rare reported. Herein, we report a facile one-pot hydrothermal method for the large-scale production of a novel composite of reduced graphene oxide (RGO) and cubic self-assembled FeS<sub>2</sub>. The structure and morphology measurements revealed that the prepared composite has interconnected networks of reduced graphene oxide sheets with well-dispersed microparticles composed of small-size cubic FeS<sub>2</sub> crystals. The composite exhibited superior anode performance including high reversible capacity and stable cyclability as an anode material for LIBs.

## 2. Experimental

### 2.1 Synthesis of graphene oxide (GO)

Graphene oxide suspension (5.6 mg mL<sup>-1</sup>) was prepared by Hummer's method.<sup>34</sup> In a typical preparation, 0.5 g of natural graphite powder (Sigma Aldrich, 5–20 μm), 0.5 g of NaNO<sub>3</sub> (AR, Damao Chemicals, Tianjin), and 23 mL of concentrated

H<sub>2</sub>SO<sub>4</sub> (AR, Damao Chemicals, Tianjin) were stirred together in an ice water bath. Then, 3.0 g of KMnO<sub>4</sub> (AR, Damao Chemicals, Tianjin) were slowly added into the solution. The solution was transferred to a 35 ± 5 °C water bath and stirred for 1.0 h to form a thick paste. Afterwards, 40 mL of water were slowly added into the paste and stirred for another 30 min, at the same time, the solution was continuously heated to 90 ± 5 °C. Subsequently, 100 mL of water was added, followed by the addition of 3 mL 30% H<sub>2</sub>O<sub>2</sub> (AR, Damao Chemicals, Tianjin) to stop the reaction. The color of the solution turned from dark brown to yellow. The obtained warm solution were filtered and washed with DI water until the pH reached at 7.0. Finally, the GO suspension was obtained via the dispersion of filter cake in water by mechanical agitation and ultrasonication for 2 h and following the centrifugation at 4500 rpm for 15 min to remove the aggregated GO.

## 2.2 Synthesis of FeS<sub>2</sub>/RGO composite

The synthesis of FeS<sub>2</sub>/RGO composite was carried out in a Teflon-lined stainless steel autoclave at 40 mL capacity. In a typical procedure, 1.35 g FeCl<sub>3</sub>·6H<sub>2</sub>O (AR, Damao Chemicals, Tianjin) were dissolved in 10 ml DI water and were dropwisely added into 15 mL of GO suspension under magnetic stirring. Keeping stirred for 30 min, another 10 mL aqueous solution containing 0.38 g (NH<sub>2</sub>)<sub>2</sub>CS (AR, Damao Chemicals, Tianjin) were dropwisely added into the mixture. After 30 min stirring, the mixture was transferred into the Teflon-lined stainless steel autoclave and maintained at 180 °C for 12 h. Finally, the autoclave was cooled down to room temperature. The resulting solid products were collected and washed with DI water for several times, followed by freeze-drying for 10 h before further characterization. For comparison, pristine FeS<sub>2</sub> and pure RGO were prepared by the same procedure with the absence of GO suspension and FeS<sub>2</sub>, respectively. For the FeS<sub>2</sub>/RGO mixture, it was obtained by physically grinding the mixtures of pristine FeS<sub>2</sub> and pure RGO at required mass ratio for half an hour.

## 2.3 Physical characterizations

The phase structure of the products was measured by powder X-ray diffraction (XRD) experiments on a D-MAX 2200 VPC diffractometer with CuKα radiation (λ = 1.54056 Å). Raman spectrum was performed on a micro Raman system (Renishaw, in Via). TGA analysis of the products was carried out by Thermogravimetry coupled with Fourier transform infrared spectrometry (TG-IR, Netzsch/Bruke). Scanning electron microscopic (SEM) measurements were conducted on a Quanta 400/INCA/HKL scanning electron microscopy and Transmission electron microscopic (TEM) measurements were examined on a Tecnai™ G2 F30 transmission electron microscopy at 300 kV. The X-ray photoelectron spectroscopy (XPS) analysis was carried out on an ESCALAB 250 system.

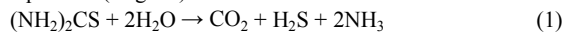
## 2.4 Electrochemical measurements

The FeS<sub>2</sub>/RGO composite electrodes were fabricated by mixing 80 wt% as prepared active material (practical FeS<sub>2</sub>/RGO composite), 10 wt% acetylene black and 10 wt% polytetrafl-uoroethylene (PVDF). The electrode films were punched into a diameter of 14 mm. The electrolyte solution consisted of 1.0 M LiPF<sub>6</sub> in 1:1 (volume) ethylene carbonate and dimethyl carbonate (EC/DMC) (LBC305-1, Shenzhen Capchem Technology Co. LTD, China). The cells assembled with 2032-type coin cell hardware were prepared in the glove box filled with high pure Ar gas. The lithium metal foils were

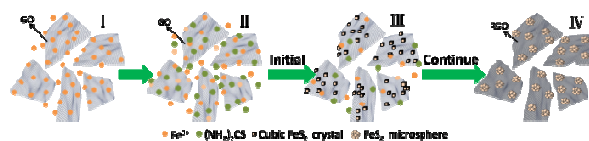
used as both the counter and reference electrodes. The sealed cells were then taken out of the glove box and placed in a battery testing system (Shenzhen Newware Battery Co., China). The cells were galvanostatically charged and discharged between 0.01 V and 3 V versus metallic lithium at room temperature after aging for more than 10 h. The cell capacity was calculated based on the weight of active material. The cyclic voltammograms (CVs) in the voltage range of 0.01 V to 3.0 V (vs. Li/Li<sup>+</sup>) at a scan rate of 0.1 mV s<sup>-1</sup> and the electrochemical impedance spectroscopy (EIS) by applying a perturbation voltage of 5 mV in a frequency range of 100 kHz to 100 mHz were tested on a ZAHNER IM6ex electrochemistry workstation (Germany).

## 3. Results and discussion

Scheme 1 illustrates the formation process of the FeS<sub>2</sub>/RGO composite in our experiment. Firstly, Fe<sup>3+</sup> were absorbed on the surface of GO via electrostatic interactions when FeCl<sub>3</sub>·6H<sub>2</sub>O aqueous solution was dropwisely added into GO suspension under magnetic stirring (stage □). Secondly, (NH<sub>2</sub>)<sub>2</sub>CS solution was dropped into the mixture under continuously magnetic stirring to be dispersed homogeneously (stage □). In initial hydrothermal process at 180 °C, H<sub>2</sub>S was produced by hydrolytic reaction of (NH<sub>2</sub>)<sub>2</sub>CS and reacted with Fe<sup>3+</sup> to form small cubic FeS<sub>2</sub> crystals via the following equations (stage □):



Usually, the formation of cubic FeS<sub>2</sub> crystal depends strongly on the surfactants and pH value in reaction system and especially the content of S precursor.<sup>18, 35, 36</sup> It has been reported that excess sulfur source benefits to form well-defined FeS<sub>2</sub> crystals without sulfur deficient phase and the surfactants act as a capping agent polymer of which the oxygen atoms strongly bind to the certain facets and thus favour the formation of crystals with truncated corner.<sup>18</sup> At this stage, GO with a lot of chemical functional groups such as -CO, -COOH and -OH acts as both surfactant and accelerator, prompting the hydrolytic reaction of (NH<sub>2</sub>)<sub>2</sub>CS to produce excess sulfur source and favoring the formation of cubic pyrite FeS<sub>2</sub> crystals. With the reaction continuing, small cubic FeS<sub>2</sub> crystals grow up via Ostwald ripening (stage □). Simultaneously, GO sheets are reduced to RGO sheets under high temperature and high pressure of hydrothermal condition.<sup>37</sup> Due to the reduction of chemical functional groups such as -CO, -COOH and -OH, the role of RGO as surfactant disappeared. To keep the reaction being stable, the grown FeS<sub>2</sub> crystals have a tendency to assemble into microparticles. Finally, novel composite of RGO and FeS<sub>2</sub> microparticles consisted of cube-shaped particles are obtained. The uniform mixture and interaction of FeS<sub>2</sub> microparticles and RGO platelets prevents both the aggregation of FeS<sub>2</sub> particles and the restacking of RGO sheets, which likely enhances the cyclability.<sup>38</sup>



Scheme 1 The illustration of the formation of FeS<sub>2</sub>/RGO composite.

Fig. 1a shows the power X-ray diffraction (XRD) patterns of

the as-synthesized pristine  $\text{FeS}_2$ , pure RGO and  $\text{FeS}_2/\text{RGO}$  composite. The dominant diffraction peaks corresponding to  $\text{FeS}_2$  can be indexed to the standard cubic phase  $\text{FeS}_2$  (JCPDS card No. 42-1340) with a space group of Pa-3 (205), which is pyrite  $\text{FeS}_2$ . The peaks of XRD pattern are very sharp, indicating that the  $\text{FeS}_2$  crystallized well. No obvious peaks at  $12.4^\circ$  corresponding to an interlayer space of 0.776 nm for GO can be observed, suggesting that GO has been reduced to RGO. In particular, the (002) characteristic diffraction peak at  $25^\circ$  of RGO is too weak and broad to be observed, implying that RGO are effectively separated with disordered stacking and less agglomeration in the as prepared composite due to the inclusion of cubic phase  $\text{FeS}_2$ . However, pristine  $\text{FeS}_2$  is not a single phase. It includes two phases of marcasite and pyrite. The marcasite  $\text{FeS}_2$  is metastable and tends to transform to pyrite  $\text{FeS}_2$  under hydrothermal process.<sup>39</sup> Therefore, according to the XRD results, the additional GO can likely restrain the growth of marcasite during the hydrothermal process, act as accelerator to benefit the formation of pure pyrite  $\text{FeS}_2$  in the final products. To determine actual weight of active materials, we did TGA analysis of as prepared  $\text{FeS}_2/\text{RGO}$  composite after the freeze-drying process. From the TGA results shown Fig. 3a, one can find that there exists rather high content ( $\sim 23\%$ ) of absorbed water in the as prepared  $\text{FeS}_2/\text{RGO}$  composite. Considering that  $\text{FeS}_2$  will transform into  $\text{Fe}_2\text{O}_3$  due to oxidation effect, we infer that the weight of  $\text{FeS}_2$  and RGO is 65% and 12%. In our experiment, the weight of the freeze-drying products is about 0.45g, thus the effective active materials is about 0.34g according to the TGA result, which is very closed to the theoretical value of  $\text{FeS}_2$  (0.3g), indicating a high yield of the preparation.

Fig. 1b shows the Raman spectra to confirm the chemical composition of  $\text{FeS}_2/\text{RGO}$  composite. Obvious Raman peaks between 200 and  $450\text{ cm}^{-1}$  correspond to  $\text{FeS}_2$  crystals. The peaks located at 336, 370 and  $423\text{ cm}^{-1}$  are attributed to Eg, Ag, and Tg mode of  $\text{FeS}_2$  crystal, respectively.<sup>35, 40, 41</sup> In addition, two peaks at 1334 and  $1595\text{ cm}^{-1}$  for RGO can be observed. The peak at  $1334\text{ cm}^{-1}$  assigned to the D-band originates from defects in the hexagonal  $sp^2$  carbon network, while the one at  $1595\text{ cm}^{-1}$  assigned to the G-band originates from the stretching motion of  $sp^2$  carbon pairs and reflects the structural intensity of the  $sp^2$ -hybridized carbon atom.<sup>42</sup> Moreover, compared with the intensity ratio (1.19) of I(D)/I(G) for GO, the ratio of  $\text{FeS}_2/\text{RGO}$  composite increased to 1.52. The increase in the I(D)/I(G) in  $\text{FeS}_2/\text{RGO}$  composite can be attributed to a substantial decrease of the oxygen-functional groups and an increase of edge planes and disordered structure on the RGO. The  $\text{FeS}_2/\text{RGO}$  composite was further evaluated by XPS analysis. From the full scan spectrum (not shown here), it can be deduced that the surface of  $\text{FeS}_2/\text{RGO}$  composite consisted of iron, sulfur, oxygen, and carbon.<sup>43</sup> The Fe 2p<sub>3/2</sub> binding energy of 707.22 eV is the characteristic of pyrite (Fig. 1c). The S 2p<sub>3/2</sub> and S 2p<sub>1/2</sub> peaks at 162.82 and 164.05 eV, respectively (Fig. 1d), are consistent with the sulfur binding energy in bulk pyrite.<sup>40, 42</sup>

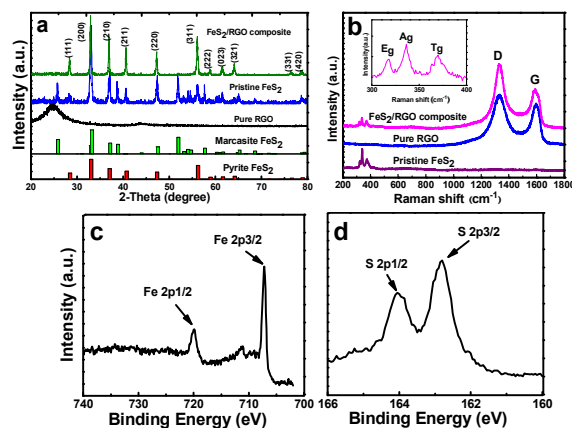


Fig. 1 (a) XRD patterns of pristine  $\text{FeS}_2$ , pure  $\text{FeS}_2$  and  $\text{FeS}_2/\text{RGO}$  composite at 30 kV and 30 mA, (b) Raman spectra of pristine  $\text{FeS}_2$ , pure RGO and  $\text{FeS}_2/\text{RGO}$  composite and (c, d) XPS spectra of the  $\text{FeS}_2/\text{RGO}$  composite.

The morphology and structure of the  $\text{FeS}_2/\text{RGO}$  composite were characterized by SEM and TEM. Fig. 2a and Fig. 2b show typical SEM images of the  $\text{FeS}_2/\text{RGO}$  composite, demonstrating that the prepared sample has interconnected networks of reduced graphene oxide sheets and  $\text{FeS}_2$  microparticles with the diameter ranging from 0.5  $\mu\text{m}$  to 1  $\mu\text{m}$ . The surface of microparticle was rough and assembled by cube-shaped building blocks at 200-300 nm which can be clearly observed under high magnification (see inset of Fig. 2b). The results reveal that the  $\text{FeS}_2$  microparticles are self-assembled from cubic  $\text{FeS}_2$  particle with small size. This unique structure offers large interfacial area and reduced the pathway for  $\text{Li}^+$ /electron transports, benefiting rapid diffusion kinetics for lithium storage to enhance the anode performance. Especially, those  $\text{FeS}_2$  microparticles are dispersed uniformly on the RGO nanosheets and the RGO nanosheets are crumpled to form plenty of channels (see Fig. S1 in Electronic Supplementary Information). Such an interesting compound structure is suggested helpful in buffering the large volume variation of electroactive material based on conversion reaction during  $\text{Li}^+$  insertion/extraction, depressing capacity fading. In contrast, the SEM image (see Fig. 2c) from pristine  $\text{FeS}_2$  is irregular. Figure 2d and 2e show typical TEM images of  $\text{FeS}_2/\text{RGO}$  composite. It can be found that  $\text{FeS}_2$  microparticles are uniformly anchored on the wrinkled RGO nanosheets. The sharp SAED pattern (inset of Fig. 2e), taken from the center of individual cube-shaped  $\text{FeS}_2$  particle, indicates that it has a well-crystallized structure. In a high resolution TEM (HRTEM) image taken from the edge of a cube-shaped  $\text{FeS}_2$  particle (Fig. 2f), the lattice fringes are clearly visible with a spacing of 0.230 nm, which is in good agreement with the spacing of the (211) plane of  $\text{FeS}_2$  (JCPDS card No.41-1340). The results imply that the addition of GO played a key role on the formation of  $\text{FeS}_2$  microparticles consisted of small size cubes.

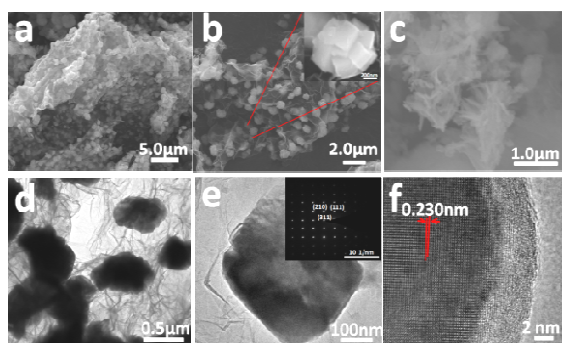
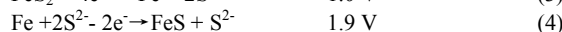


Fig. 2 (a, b) SEM images of FeS<sub>2</sub>/RGO composite and (c) pristine FeS<sub>2</sub>, (d, e) TEM images, the inset of (e) is the electron diffraction spectrum of FeS<sub>2</sub>/RGO composite and (f) HRTEM image of the FeS<sub>2</sub>/RGO composite.

Electrochemical performance of the FeS<sub>2</sub>/RGO composite was evaluated in half-cell configuration in which metallic lithium acts as counter and reference electrodes at room temperature. The CV measurements were firstly performed to determine the reduction and oxidation potentials of FeS<sub>2</sub>/RGO composite. As shown in Fig. 3b, the CV curve of FeS<sub>2</sub>/RGO composite (black line) exhibits one sharp reduction peak at about 1.0 V and two oxidation peaks at about 1.9 V and 2.5 V, respectively. In the first cycle, these peaks are attributed to the following reactions:<sup>15</sup>



The small shoulder peak at 0.8 V is due to the formation of SEI film<sup>44, 45</sup> in the first cycle. After the first cycle, the reduction peak moved to about 1.4 V and additional peak at 2.0 V appeared, suggesting an irreversible phase transformation due to the formation of S and Li<sub>2</sub>S. Compared with pristine FeS<sub>2</sub>, the intensities of the oxidation and reduction peaks for FeS<sub>2</sub>/RGO composite are much stronger, implying that FeS<sub>2</sub>/RGO composite has high reversible capacity. Moreover, the second and onward CV curves are well-overlapped. The deviation in the peak position and intensity in the subsequent cycles reveals the possible existence of irreversible activation process of active materials due to polarization barrier. Hence, more steady CV results indicate highly reversible conversion of FeS<sub>2</sub>/RGO composite instead of poor reversibility of pristine FeS<sub>2</sub>.

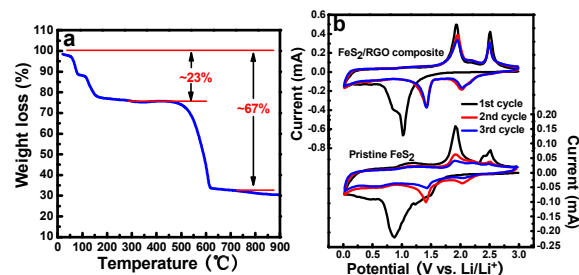


Fig. 3 (a) TGA curves of FeS<sub>2</sub>/RGO, (b) the CV curves of the pristine FeS<sub>2</sub> and FeS<sub>2</sub>/RGO composite at the scan rate of 0.1 mVs<sup>-1</sup>.

Fig. 4a shows the first, second, third and 60<sup>th</sup> charge–discharge curves of the FeS<sub>2</sub>/RGO composite electrode at a current density of 100 mA g<sup>-1</sup>. There exists a long voltage plateau near 1.5V for the electrode in the first discharge cycle, but it gradually reduces in the subsequent cycles. This phenomenon

reflects the initial irreversible capacity loss which is mainly due to the formation of SEI film.<sup>46</sup> The initial discharge and charge capacities of the FeS<sub>2</sub>/RGO hybrid electrode were 1428 and 1148 mAh g<sup>-1</sup>, respectively, which led to an irreversible capacity loss of 280 mAh g<sup>-1</sup> and a coulombic efficiency of 80.4 %. The irreversible capacity loss arising during the first cycle is likely due to the incomplete decomposition of Li<sub>2</sub>S and the difficult dissolution of SEI film.<sup>47</sup> Although the coulombic efficiency of the 1st cycle is not high enough for FeS<sub>2</sub>/RGO composite, it is improved greatly upon cycling. For example, during the 2<sup>nd</sup> cycle, a discharge capacity of 1272 mAh g<sup>-1</sup> and a charge capacity of 1173 mAh g<sup>-1</sup> were exhibited, indicating an increased coulombic efficiency of 92.2 %. At the 3<sup>rd</sup> cycle, the value increases to 96.7 %, and from the 6<sup>th</sup> cycle, it maintained about at 98 %.

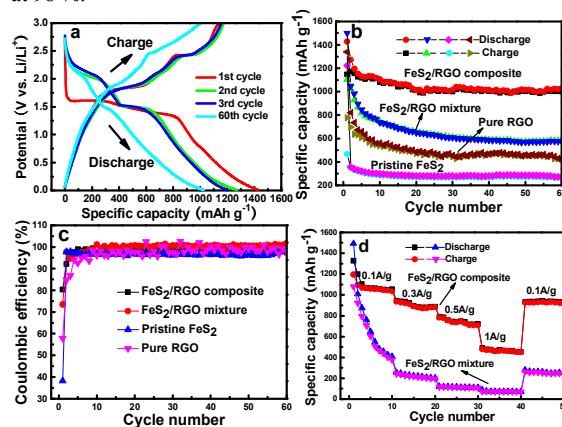


Fig. 4 (a) Discharge-charge curves of FeS<sub>2</sub>/RGO composite at a current density of 100 mA g<sup>-1</sup>, (b) cycling performance and (c) coulombic efficiencies of pristine FeS<sub>2</sub>, pure RGO, FeS<sub>2</sub>/RGO mixture and FeS<sub>2</sub>/RGO composite at a current density of 100 mA g<sup>-1</sup>, (d) rate performance of FeS<sub>2</sub>/RGO mixture and FeS<sub>2</sub>/RGO composite at different current densities.

Fig. 4b shows the cycling performance of the FeS<sub>2</sub>/RGO composite, FeS<sub>2</sub>/RGO mixture, pure RGO and pristine FeS<sub>2</sub> electrodes. As can be seen, the cycling performance of FeS<sub>2</sub>/RGO composite material is apparently superior to those of FeS<sub>2</sub>/RGO mixture, pure RGO and pristine FeS<sub>2</sub>. The initial discharge and charge capacities for FeS<sub>2</sub>/RGO composite, FeS<sub>2</sub>/RGO mixture, pure RGO and pristine FeS<sub>2</sub> are 1428 and 1147, 1499.9 and 1102.7, 1340.2 and 775.9, 1223.3 and 466.9 mAh g<sup>-1</sup>, respectively, corresponding to the coulombic efficiencies of 80.3%, 73.52%, 57.89% and 38.17% (shown in Fig. 4c) with the cut-off voltage of discharge-charge process between 0.01V-3.0V at a rate of 100 mA g<sup>-1</sup>. After 60 cycles, a high charge capacity of 1101.41 mAh g<sup>-1</sup> for FeS<sub>2</sub>/RGO hybrid material can be retained and only 584.42, 417.25 and 264.01 mAh g<sup>-1</sup> are maintained for FeS<sub>2</sub>/RGO mixture, pure RGO and pristine FeS<sub>2</sub>, respectively. The capacity of FeS<sub>2</sub>/RGO mixture is better than those of pure RGO and pristine FeS<sub>2</sub> but worse than that of FeS<sub>2</sub>/RGO composite. This indicated that RGO played an important role to improve the cycling performance and the coulombic efficiency of the electrodes. The capacity of the FeS<sub>2</sub>/RGO composite is also higher than graphite (372 mAh g<sup>-1</sup>) and previous reported FeS<sub>2</sub>-based composites such as iron sulfide-embedded carbon microsphere,<sup>13</sup> FeS<sub>2</sub>/CNT micro-spherical material,<sup>14</sup> FeS<sub>2</sub>/C composite,<sup>26</sup> cubic pyrite/nitrogen-doped graphene composite<sup>27</sup> and other

FeS<sub>2</sub>-based materials. Table 1 shows the comparison of different FeS<sub>2</sub>-based materials in cycling performance at various testing situations reported in recent years (see the Electronic Supplementary Information). Particularly, it is much higher than the theoretical value of FeS<sub>2</sub>/RGO composite, which is calculated to be 947 mAh g<sup>-1</sup> according to the reference value of 890 mAh g<sup>-1</sup> for FeS<sub>2</sub> and 1260 mAh g<sup>-1</sup> for RGO.<sup>48</sup> The phenomenon that the practical capacities of the composites were beyond their theoretical values was reported by many researches.<sup>38, 49-55</sup> The graphene matrix can effectively buffer the volume variation during the Li<sup>+</sup> insertion and extraction process and serve as conductive medium for electron transfer during the discharge and charge process.<sup>56</sup> On the other hand, it is inferred that the measured high capacity of the FeS<sub>2</sub>/RGO composite may due to strong synergistic effect between FeS<sub>2</sub> microparticles self-assembled from small size cubes and the wrinkled RGO nanosheets.<sup>27, 30</sup> Moreover, the disordered and interconnected structure of RGO in FeS<sub>2</sub>/RGO composite may provide more space or electroactive sites for lithium storage than the theoretical value of pure RGO in good order.<sup>57-59</sup> Compared with individual cubic pyrite/nitrogen-doped graphene composite,<sup>27</sup> the FeS<sub>2</sub> microparticles self-assembled from the cubes may hold more defects including the dislocations, vacancies and distortions in the intersection of adjacent FeS<sub>2</sub> cubes, which facilitates more intercalation of lithium ions.<sup>55</sup> Further reasons for unusual high capacity of the FeS<sub>2</sub>/RGO composite are also in progress.

Besides the high specific capacity and good cyclability, the rate capability is also a very important property for electrode materials. To evaluate the rate capability, the sample of FeS<sub>2</sub>/RGO composite and FeS<sub>2</sub>/RGO mixture electrodes were cycled at various current densities (0.1–1.0 A g<sup>-1</sup>) and the results are shown in Fig. 4d. It is clear that FeS<sub>2</sub>/RGO composite sample shows much more excellent high rate capability at each rate than FeS<sub>2</sub>/RGO mixture sample. For example, at high current rate of 1000 mA g<sup>-1</sup>, FeS<sub>2</sub>/RGO composite still delivered a favorable reversible capacity of about 500 mAh g<sup>-1</sup> and exhibited good capacity retention. While FeS<sub>2</sub>/RGO mixture just retained a capacity of 90 mAh g<sup>-1</sup>, which implies more efficient solid-state diffusion of lithium in FeS<sub>2</sub>/RGO hybrid than that in FeS<sub>2</sub>/RGO mixture. More importantly, after the high rate charge–discharge cycles, an average discharge capacity of as high as 920 mA h g<sup>-1</sup> can be still maintained when the current density was reduced to 100 mA g<sup>-1</sup>, suggesting a good structural stability of the FeS<sub>2</sub>/RGO composite electrode.

To gain more insight into the superior electrochemical performance of FeS<sub>2</sub>/RGO composite compared with other reported results in literature, EIS measurements were performed after the rate capability test. The respective impedance spectra (see Fig. 5) were similar, composed of one semicircle component at high frequency due to charge-transfer resistance at the electrode/electrolyte interface and a line following at low frequency related to the Warburg impedance of the lithium-ion diffusion within electrodes. In particular, the Nyquist plots shown that the diameter of the semicircle for the FeS<sub>2</sub>/RGO composite in the high–medium frequency region was much smaller than that of other materials, suggesting the lower contact and charge-transfer resistance of the FeS<sub>2</sub>/RGO composite.

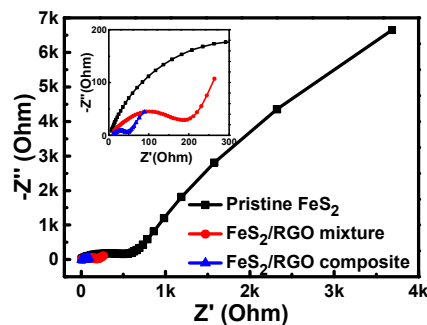


Fig. 5 Nyquist plots of pristine FeS<sub>2</sub>, FeS<sub>2</sub>/RGO mixture and FeS<sub>2</sub>/RGO composite.

The above results demonstrate high capacity, good cyclability and excellent rate capability of FeS<sub>2</sub>/RGO composite as a good candidate for anode materials in high power LIBs. In the prepared FeS<sub>2</sub>/RGO composite, the following four advantages are integrated together due to its unique structure. Firstly, pyrite FeS<sub>2</sub> cubes with high-quality not only promote uniform deliveries of electrons and ions but also shorten Li<sup>+</sup> insertion/extraction pathways due to their single-crystal nature. Secondly, the cube-shaped nature of the FeS<sub>2</sub> particles enlarges FeS<sub>2</sub>/electrolyte contact area and further promotes the transportation of lithium ions because more accessible active sites on exposed crystallographical plane are contacted with the electrolyte solution. Thirdly, the effectively separated RGO nanosheets due to the inclusion of FeS<sub>2</sub> microparticles consisted of small size cube enhance the synergistic effect between cubic FeS<sub>2</sub> and RGO nanosheets, which improve reversible capacity. Fourthly, the highly flexible and stable RGO nanosheets act as a substrate to accommodate the volume changes during the electrochemical cycling, thereby retaining the morphology and structural integrity of the electrode materials, but also a conducting agent to provide efficient electrical and ionic transfer channels, which contribute to the much improved transfer rate of Li<sup>+</sup> ions and electron conductivity of the active material, thereby improving the cycling and rate performance of FeS<sub>2</sub>/RGO composite. As a result, FeS<sub>2</sub>/RGO composite demonstrates to own outstanding electrochemical performance.

#### 4. Conclusions

A novel composite consisted of RGO and well-dispersed FeS<sub>2</sub> microparticles (FeS<sub>2</sub>/RGO) by one-pot hydrothermal method. The characterization of structure and morphology reveals that the FeS<sub>2</sub>/RGO composite has interconnected networks of reduced graphene oxide sheets and the FeS<sub>2</sub> microparticle which is composed of small-size cubes. The unique structure of FeS<sub>2</sub>/RGO composite provides high contact area between electrolyte and electrode, efficient electron conducting pathway, perfect protection against the volume change of anode materials and excellent electrical conductivity of the overall electrode during electrochemical processes as well as enhanced synergistic effect between cubic FeS<sub>2</sub> and RGO. As a result, FeS<sub>2</sub>/RGO composite exhibits superior anode performance compared with reported materials in terms of the capacity, cycling and rate capability and stability. It implies that FeS<sub>2</sub>/RGO composite can be potentially applied in high-performance LIB.

#### Acknowledgements

This work was supported by the National Natural Science

Foundation of China (Grant No. 11204262), the Open Fund based on innovation platform of Hunan colleges and universities (No.12K045).

## Notes and references

<sup>a</sup> Key Laboratory of Quantum Engineering and Micro-Nano Energy Technology, School of Materials, Optoelectronics and Physics, Xiangtan University, Xiangtan 411105, China. E-mail: xlv@xtu.edu.cn (X.L.W.)

<sup>b</sup> Advanced Energy Materials Research Laboratory, School of Physics and Engineering, Sun Yat-sen University, Guangzhou 510275, China. fax: +86-20-84113369; Tel: +86-20-84036736; stspk@mail.sysu.edu.cn (P.K.S.)

- 1 A. Hu, X. Chen, Y. Tang, Q. Tang, L. Yang and S. Zhang, *Electrochem. Commun.*, 2013, 28, 139-142.
- 2 L. Shen, H. Song, H. Cui, X. Wen, X. Wei and C. Wang, *CrystEngComm*, 2013, 15, 9849-9854.
- 3 P. Poizot, S. Laruelle, S. Grugeon and L. D. J.-M. Tarascon, *Nature*, 2000, 407, 496-499.
- 4 M. V. Reddy, T. Yu, C. H. Sow, Z. X. Shen, C. T. Lim, G. V. Subba Rao and B. V. R. Chowdari, *Adv. Funct. Mater.*, 2007, 17, 2792-2799.
- 5 R. Demir-Cakan, Y.-S. Hu, M. Antonietti, J. Maier and M.-M. Titirici, *Chem. Mater.*, 2008, 20, 1227-1229.
- 6 Y. Shi, B. Guo, S. A. Corr, Q. Shi, Y.-S. Hu, K. R. Heier, L. Chen, R. Seshadri and G. D. Stucky, *Nano Lett.*, 2009, 9, 4215-4220.
- 7 A. Débart, L. Dupont, R. Patrice and J. M. Tarascon, *Solid State Sci.*, 2006, 8, 640-651.
- 8 J. Xiao, D. Choi, L. Cosimbescu, P. Koech, J. Liu and J. P. Lemmon, *Chem. Mater.*, 2010, 22, 4522-4524.
- 9 H. Liu, D. Su, G. Wang and S. Z. Qiao, *J. Mater. Chem.*, 2012, 22, 17437-17440.
- 10 B. Wang, J. Park, D. Su, C. Wang, H. Ahn and G. Wang, *J. Mater. Chem.*, 2012, 22, 15750-15756.
- 11 X. Xie, D. Su, S. Chen, J. Zhang, S. Dou and G. Wang, *Chem. Asian J.*, 2014, 9, 1611-1617.
- 12 D. Zhang, G. Wu, J. Xiang, J. Jin, Y. Cai and G. Li, *Materials Science and Engineering B*, 2013, 178, 483-488.
- 13 B. Wu, H. Song, J. Zhou and X. Chen, *Chem. Commun.*, 2011, 47, 8653-8655.
- 14 L. Liu, Z. Yuan, C. Qiu and J. Liu, *Solid State Ionics*, 2013, 241, 25-29.
- 15 S. Kar and S. Chaudhuri, *Chem. Phys. Lett.*, 2004, 398, 22-26.
- 16 P. Gao, Y. Xie, L. Ye, Y. Chen and Q. Guo, *Crystal Growth & Design*, 2006, 6, 583-587.
- 17 X. Feng, X. He, W. Pu, C. Jiang and C. Wan, *Ionics*, 2007, 13, 375-377.
- 18 D. Wang, Q. Wang and T. Wang, *CrystEngComm*, 2010, 12, 755-761.
- 19 D. Wang, M. Wu, Q. Wang, T. Wang and J. Chen, *Ionics*, 2011, 17, 163-167.
- 20 M. Li, Q. Yao, G. Zhou, X. Qu, C. Mu and S. Fu, *CrystEngComm*, 2011, 13, 5936-9542.
- 21 X. Qiu, M. Liu, T. Hayashi, M. Miyauchi and K. Hashimoto, *Chem. Commun.*, 2013, 49, 1232-1234.
- 22 L. Li, M. Caban-Acevedo, S. N. Girard and S. Jin, *Nanoscale*, 2014, 6, 2112-2118.
- 23 W. L. Liu, X. H. Rui, H. T. Tan, C. Xu, Q. Y. Yan and H. H. Hng, *RSC Adv.*, 2014, 4, 48770-48776.
- 24 Y. Wang, X. Qian, W. Zhou, H. Liao and S. Cheng, *RSC Adv.*, 2014, 4, 36597-36602.
- 25 S. X. Yu, L. W. Yang, Y. Tian, P. Yang, F. Jiang, S. W. Hu, X. L. Wei and J. X. Zhong, *J. Mater. Chem. A*, 2013, 1, 12750-12758.
- 26 D. Zhang, Y. J. Mai, J. Y. Xiang, X. H. Xia, Y. Q. Qiao and J. P. Tu, *J. Power Sources*, 2012, 217, 229-235.
- 27 W. Qiu, J. Xia, H. Zhong, S. He, S. Lai and L. Chen, *Electrochim. Acta*, 2014, 137, 197-205.
- 28 J. Yao, X. Shen, B. Wang, H. Liu and G. Wang, *Electrochem. Commun.*, 2009, 11, 1849-1852.
- 29 Y. Sun, X. Hu, W. Luo and Y. Huang, *J. Phys. Chem. C*, 2012, 116, 20794-20799.
- 30 X. Zhu, Y. Zhu, S. Murali, M. D. Stoller and R. S. Ruoff, *ACS nano*, 2011, 5, 3333-3338.
- 31 L. Shen, C. Yuan, H. Luo, X. Zhang, S. Yang and X. Lua, *Nanoscale*, 2011, 3, 572-574.
- 32 X. Xin, X. Zhou, F. Wang, X. Yao, X. Xu, Y. Zhu and Z. Liu, *J. Mater. Chem.*, 2012, 22, 7724-7730.
- 33 J. Zhu, Y. Li, S. Kang, X. Wei and P. K. Shen, *J. Mater. Chem. A*, 2014, 2, 3142-3147.
- 34 W. S. Hummers Jr and R. E. Offeman, *J. Am. Chem. Soc.*, 1958, 80, 1339.
- 35 X. Chen, Z. Wang, X. Wang, J. Wan, J. Liu and Y. Qian, *Inorg. Chem.*, 2005, 44, 951-954.
- 36 L. Zhu, B. Richardson, J. Tanumihardja and Q. Yu, *CrystEngComm*, 2012, 14, 4188-4195.
- 37 Y. Zhou, Q. Bao, L. A. L. Tang, Y. Zhong and K. P. Loh, *Chem. Mater.*, 2009, 21, 2950-2956.
- 38 X. Zhu, Y. Zhu, S. Murali, M. D. Stoller and a. R. S. Ruoff, *ACS nano*, 2011, 5, 3333-3338.
- 39 A. M. Golsheikh, N. M. Huang, H. N. Lim, C. H. Chia, I. Harrison and M. R. Muhamad, *Chem. Eng. J.*, 2013, 218, 276-284.
- 40 C. Wadia, Y. Wu, S. Gul, S. K. Volkman, J. Guo and A. P. Alivisatos, *Chem. Mater.*, 2009, 21, 2568-2570.
- 41 K. N. Kudin, B. Ozbas, H. C. Schniepp, R. K. Prud'homme, I. A. Aksay and R. Car, *Nano Lett.*, 2008, 8, 36-41.
- 42 P. Velasquez, D. Leinen, J. Pascual, J. R. Ramos-Barrado and P. Grez, *J. Phys. Chem. B*, 2005, 109, 4977-4988.
- 43 E. J. Kim and B. Batchelor, *Mater. Res. Bull.*, 2009, 44, 1553-1558.
- 44 L. A. Montoro and J. M. Rosolen, *Solid State Ionics*, 2003, 159, 233-240.
- 45 L. Fei, Q. Lin, B. Yuan, G. Chen, P. Xie, Y. Li, Y. Xu, S. Deng, S. Smimov and H. Luo, *ACS Appl. Mater. Inter.*, 2013, 5, 5330-5335.
- 46 F. Jiang, L. Yang, Y. Tian, P. Yang, S. Hu, K. Huang, X. Wei and J. Zhong, *Ceram. Int.*, 2014, 40, 4297-4304.
- 47 H. Wang, Q. Pan, Y. Cheng, J. Zhao and G. Yin, *Electrochim. Acta*, 2009, 54, 2851-2855.
- 48 P. Lian, X. Zhu, S. Liang, Z. Li, W. Yang and H. Wang, *Electrochim. Acta*, 2010, 55, 3909-3914.
- 49 Z.-S. Wu, W. Ren, L. Wen, L. Gao, J. Zhao, Z. Chen, G. Zhou, F. Li and H.-M. Cheng, *ACS NANO*, 2010, 4, 3187-3194.
- 50 K. Chang, Z. Wang, G. Huang, H. Li, W. Chen and J. Y. Lee, *J. Power Sources*, 2012, 201, 259-266.
- 51 J. Lin, Z. Peng, C. Xiang, G. Ruan, Z. Yan, D. Natelson and J. M. Tour, *ACS NANO*, 2013, 7, 6001-6006.
- 52 B. Lung-Hao Hu, F. Y. Wu, C. T. Lin, A. N. Khlobystov and L. J. Li, *Nat. Commun.*, 2013, 4, 1687-1694.
- 53 L. Su, Z. Zhou, X. Qin, Q. Tang, D. Wu and P. Shen, *Nano Energy*, 2013, 2, 276-282.
- 54 D. Kong, H. He, Q. Song, B. Wang, W. Lv, Q.-H. Yang and L. Zhi, *Energy Environ. Sci.*, 2014, 7, 3320-3325.
- 55 J. Wang, J. Liu, D. Chao, J. Yan, J. Lin and Z. X. Shen, *Adv. Mater.*, 2014, 26, 7162-7169.
- 56 D. Su, H. J. Ahn and G. Wang, *Chem. Commun.*, 2013, 49, 3131-3133.
- 57 E. Yoo, J. Kim, Eiji Hosono, H.-s. Zhou, T. Kudo and I. Honma, *Nano Lett.*, 2008, 8, 2277-2282.
- 58 D. Pan, S. Wang, B. Zhao, M. Wu, H. Zhang, Y. Wang and Z. Jiao, *Chem. Mater.*, 2009, 21, 3136-3142.
- 59 G. Wang, X. Shen, J. Yao and J. Park, *Carbon*, 2009, 47, 2049-2053.